Insights into the Causes and Predictability of the 2022/23 California Flooding

Siegfried D. Schubert[12], Yehui Chang[13], Anthony M. DeAngelis[12], Young-Kwon Lim[14], Natalie P. Thomas[14], Randal D. Koster[1], Michael G. Bosilovich[1], Andrea M. Molod[1], Allison Collow[14], Amin Dezfuli[14]

[1]Global Modeling and Assimilation Office, NASA GSFC

[2]Science Systems and Applications, Inc.

[3]Goddard Earth Sciences Technology and Research II / Morgan State University

[4]Goddard Earth Sciences Technology and Research II / University of Maryland Baltimore County (UMBC)

22 Feb 2024

Corresponding Author:
Siegfried D. Schubert
Science Systems and Applications, Inc.
Lanham, MD USA
siegschu2002@yahoo.com

Submitted to Journal of Climate

Early Online Release: This preliminary version has been accepted for publication in *Journal of Climate*, may be fully cited, and has been assigned DOI 10.1175/JCLI-D-23-0696.1. The final typeset copyedited article will replace the EOR at the above DOI when it is published.

Abstract

In late December of 2022 and the first half of January 2023 an unprecedented series of atmospheric rivers (ARs) produced near record heavy rains and flooding over much of California. Here we employ the NASA GEOS AGCM run in a "replay" mode, together with more idealized simulations with a stationary wave model, to identify the remote forcing regions, mechanisms and underlying predictability of this flooding event. In particular, the study addresses the underlying causes of a persistent positive Pacific/North American (PNA) - like circulation pattern that facilitated the development of the ARs. We show that that pattern developed in late December as a result of vorticity forcing in the North Pacific jet exit region. We further provide evidence that this vorticity forcing was the result of a chain of events initiated in mid-December with the development of a Rossby wave (as a result of forcing linked to the MJO) that propagated from the northern Indian Ocean into the North Pacific. As such, both the initiation of the event and the eventual development of the PNA depended critically on internally-generated Rossby wave forcings, with the North Pacific jet playing a key role. This, combined with contemporaneous SST (La Niña) forcing that produced a circulation response in the AGCM that was essentially opposite to the positive PNA, underscores the fundamental lack of predictability of the event at seasonal time scales. Forecasts produced with the GEOS coupled model suggests that useful skill in predicting the PNA and extreme precipitation over California was in fact limited to lead times shorter than about 3 weeks.

Accepted for publication in *Journal of Climate.* DOI 10.1175/JCLI-D-23-0696.1.

1. **Introduction**

During late December 2022 and the first half of January 2023 California was impacted by an extraordinary number of atmospheric rivers (ARs) or narrow bands of moisture (e.g., Gimeno et al. 2014) that produced heavy rains and flooding over much of the state, with the San Francisco Bay area experiencing the wettest 3-week period in 161 years[1]. The rains resulted in at least 21 deaths and property damages estimated to be $5- 7 Billion[2]. It appears that none of the world's major forecast centers issuing long-lead (seasonal) outlooks, predicted the event[3] (DeFlorio et al. 2023). This is perhaps not surprising given that the flooding occurred during La Niña conditions; wet conditions in California (though primarily southern California) are more likely to occur during moderate to strong El Niño events (Jong et al. 2016).

A number of studies have addressed the possible impacts of ENSO, the Madden-Julian Oscillation (MJO), and various sub-seasonal extratropical modes of variability such as the Pacific-North American (PNA, Wallace and Gutzler 1981) pattern, on ARs in the North Pacific. Focusing on just a few of the more recent studies, Guirguis et al. (2019) found that while ENSO plays a role in modulating the synoptic evolution of ARs and their evolution at landfall over Northern California, subseasonal climate modes of variability appear to be more influential in modulating California precipitation variability. Collow et al. (2020) showed that extreme precipitation events tied to ARs along the Washington State coast are influenced by both the MJO and ENSO. In particular, they found that extreme precipitation events are most often associated with MJO-related convection centered over the Maritime Continent, while convection over the Indian Ocean tends to discourage extreme events, though this is all modulated by ENSO's impact on the MJO's phase speed. Zhou et al. (2021), in examining the MJO's role in modulating the lifecycle of ARs in the North Pacific, showed that their origin depends on the phase of the MJO. They found a primarily eastern Asia origin when the enhanced convection tied to the MJO is over the Indian Ocean and a primarily subtropical northern Pacific origin when the enhanced convection is over the western Pacific, with MJO-related anomalous extra-tropical circulation patterns modulating AR propagation. Toride and Hakim (2022) contrasted

[1] https://www.noaa.gov/news/january-2023-was-nations-6th-warmest-on-record
[2] https://www.rms.com/newsroom/press-releases/press-detail/2023-01-25/moodys-rms-estimates-us5-7-billion-in-total-us-economic-losses-from-california-flooding
[3] https://www.cpc.ncep.noaa.gov/products/NMME/

Accepted for publication in *Journal of Climate.* DOI 10.1175/JCLI-D-23-0696.1.

MJO events that are followed by AR events with those that are not, focusing on the Pacific Northwest. They found that the primary contribution of the MJO to the ARs is the development of a ridge over the central North Pacific that facilitates moisture transport across the North Pacific – moisture that is then available for the production of AR events via extratropical variability that is uncorrelated with the MJO (such as the PNA). Fish et al. (2022) employed a clustering algorithm to identify the large-scale circulation environments most conducive to different families of AR events impacting California precipitation. They found two clusters that have a strong relationship to ENSO, with one characterized by a ridge in the Bering Sea which tends to occur during La Niña and neutral ENSO years, and the other, characterized by an extended North Pacific jet, which tends to occur during El Niño years.

The above studies make clear that the links between ARs and the various modes of low frequency climate variability are rather complicated and far from settled. While ENSO appears to be a factor, subseasonal variability such as that associated with the MJO and PNA can play a greater role. Given the diversity of ARs and their links to climate variability, we believe detailed case studies (rather than composite-type analyses) involving some of the most extreme events (or family of events) may ultimately provide more insight into the underlying causes of the events and their links to climate variability. We accordingly focus here on the physical mechanisms driving the large-scale atmospheric circulation anomalies that facilitated the development of the family of storm systems and related ARs during late December 2022 and the first half of January 2023.

Section 2 describes our approach. It relies heavily on a "regional replay" technique (Schubert et al. 2019b) developed by NASA's GMAO that, by constraining the model to reproduce the reanalysis over specified regions of the globe, helps isolate the remote geographic regions and potential physical mechanisms instrumental to the development of the flooding event. In addition, we describe supplementary experiments with a stationary wave model (SWM) that further elucidate and pinpoint the relevant forcing mechanisms. Results are presented in Section 3, starting with a brief background of the event (Section 3a). We then focus successively on the ability of the AGCM to reproduce the relevant time mean (roughly three week) flood period anomalies (Section 3b), the initiation and development of the event (Section 3c), and the ability

Accepted for publication in *Journal of Climate.* DOI 10.1175/JCLI-D-23-0696.1.

of the GEOS coupled model to predict the event (Section 3d). Discussion and conclusions are presented in Section 4.

2. The model experiments and diagnostics

a. Regional Replay with the GEOS AGCM

Our approach to isolating the remote drivers of the flooding event involves the use of regional replay (Schubert et al. 2019b), in which large ensembles of simulations with the NASA GEOS Atmospheric General Circulation Model (AGCM, Molod et al. 2015) are constrained to remain close to MERRA-2 (the Modern Era Retrospective-Analysis for Research and Applications, Version 2 [Gelaro *et al*. 2017]) over specified regions of the globe. In that way, one can assess whether the prescribed atmospheric forcing in a replayed region (e.g., the tropics) encouraged the development of anomalous atmospheric conditions outside the prescribed region, thereby identifying the replayed region as an important source of remote forcing through an atmospheric teleconnection mechanism. We should emphasize that that does not identify the nature of the forcing in the replayed region, which may be strongly influenced by internal atmospheric variability or linked with the underlying boundary conditions (i.e., SSTs). In order to assess that, we make use of SWM experiments described below. We note that the regional replay approach has already been successfully used to diagnose remote sources of a number of different extreme events in the Northern Hemisphere (Schubert et al. 2021, 2022; DeAngelis et al. 2023).

As described in Schubert et. al. (2021), the GEOS AGCM used here is essentially the same as that used to produce MERRA-2 except for two differences: (i) we run it at a coarser horizontal resolution (approximately 1°, compared to 1/2° for MERRA-2), and (ii) it uses tendency bias correction (TBC) to help alleviate some of the model's long-term biases (Chang et al. 2019)[4]. The model equations governing replay have the general form: $\frac{\partial x}{\partial t} = f(x) + \Delta x$, where $\Delta x = (\text{analysis} - \text{forecast})/6\text{hrs}$, and f(x) consists of all the dynamics and physics terms of the model. Here, Δx is recomputed every 6 hours, but applied (appropriately scaled) at each time step to the model's prognostic variables (temperature, specific humidity, horizontal winds, surface pressure).

[4]As described in Chang et al. (2019), the TBCs consist of time-averaged (over several decades) 6-hourly analysis increments (first guess forecast minus analysis) obtained from MERRA-2 reanalysis data which are added with opposite sign as additional forcing terms to the model equations.

Accepted for publication in *Journal of Climate.* DOI 10.1175/JCLI-D-23-0696.1.

The details of the replay approach can be found in Chang et al. (2019), and how that differs from nudging can be found in Schubert et al. (2022).

The runs performed for this study (Table 1) consist of regional replay simulations in which the model is constrained to remain close to MERRA-2 in the tropics (RPL_TR) and the western North Pacific (RPL_WNP) as well as runs without replay (NORPL).

In all three sets of runs, daily mean SST and sea ice concentration from MERRA-2 are prescribed everywhere across the globe (Gelaro et al. 2017). The runs are initialized in January 1980 by perturbing the atmosphere as described in Schubert et al. (2019a), precluding any impact from the initial conditions during the flood period. We note, however, that the main reason for such long simulations is to allow producing separate climatologies for each set of runs: replay can impact the long-term climatology and if not taken into account can introduce biases in the computed anomalies (Schubert et al. 2022).

Name	Time period	Replay region	Ensemble members
NORPL	Jan 1980- Jan 2023	none	45
RPL_TR	Jan 1980- Jan 2023	Tropics: 25°S-25°N	45
RPL_WNP	Jan 1980- Jan 2023	Western North Pacific: (25°N-70°N, 120E°-180°)	45
NORPL_IND	Dec 14-23, 2022 replay Dec 24-Jan 31 NORPL	Indian Ocean (10°E-120°E, 25°S-25°N)	45

Table 1: List of the AGCM experiments discussed in the text. The primary long runs (NORPL, RPL_TR, RPL_WNP) were initialized on 1 January 1980 and were forced with observed daily mean SST (SSTs are the same as those used in MERRA-2, see Gelaro et al. 2017). The NORPL_IND run was also forced with observed daily mean SST, but replayed for only 10 days, initialized from the NORPL runs on Dec 14. The perturbations to the initial conditions for each of the ensemble members were produced by taking the scaled differences between two MERRA-2 atmospheric states as described in Schubert et al. (2019a). The various replay regions are outlined in Fig. 1.

Our above choice of replay regions is designed to isolate the potential role of the tropics (RPL_TR) in forcing (via teleconnections) the relevant large scale midlatitude circulation anomalies, as well

Accepted for publication in *Journal of Climate.* DOI 10.1175/JCLI-D-23-0696.1.

as the potential role of remote upstream midlatitude forcing in the western North Pacific (RPL_WNP). Here we are especially interested in determining the extent to which a PNA-like circulation anomaly similar to that which developed in late December 2022, is generated in the AGCM simulations when given the full observed atmospheric forcing in our replay regions, as well as, with only SST forcing. In addition to the above replay runs, we perform an ensemble of replay runs of much more limited duration (NORPL_IND): these were initialized on Dec 14, 2022 from the NORPL runs and replayed over the Indian Ocean region (Fig. 1) for only 10 days, after which they ran in NORPL mode. The primary motivation for these runs is to help determine whether the positive PNA-like pattern was initiated by forcing tied to the MJO, which was active over the Indian Ocean during that time.

We shall see that a critical aspect of the positive PNA-like pattern that developed in late December of 2022 is the extension of the negative anomaly eastward onto the coast, crucial for steering the storms onto the continent. In fact, the canonical positive PNA pattern puts the North Pacific negative anomaly somewhat off the coast[5] making it less effective in producing wet conditions over land. In the following we will nevertheless, for simplicity, refer to the sequence of anomalies in the North Pacific/North American region as the positive PNA pattern, keeping in mind that it does differ in detail from the canonical pattern. We will come back to this distinction in Section 4.

b. Stationary Wave Model Experiments

We employ a stationary wave model (SWM) to help us further isolate the forcing region as well as understand the nature of the forcing: something not possible from the replay results. In particular, while the replay runs identify the general regions in which forcing of a particular teleconnection pattern may to be important, it tells us little about the nature of that forcing (e.g., is it an effective Rossby wave source (see below), or the direct response to anomalous heating?). Furthermore, short of doing a large number of AGCM replay simulations over smaller and smaller regions (something that is computationally expensive), it is difficult to pinpoint the exact location of the forcing from the replay runs.

[5] https://www.cpc.ncep.noaa.gov/products/precip/CWlink/pna/pna.loading.shtml

Accepted for publication in *Journal of Climate.* DOI 10.1175/JCLI-D-23-0696.1.

The SWM is the dry dynamical core of a full nonlinear time-dependent AGCM with rhomboidal wavenumber-30 truncation in the horizontal and 14 unevenly spaced σ levels in the vertical (Ting and Yu 1998). Following Schubert et al. (2011) and DeAngelis et al. (2023), we perform numerous SWM simulations where idealized heating or vorticity sources are imposed. Specifically, each simulation is given either idealized heat or vorticity forcing at one of many forcing locations spaced every 10° longitude and 5°latitude across the globe. The idealized forcing sources at each location have a sine-squared functional spatial structure, with horizontal scales of 10° longitude by 10° latitude for vorticity and 40° longitude by 10° latitude for heat. The vertical structure (see Liu et al 1998) of the vorticity forcing peaks in the upper troposphere (with a value of ~5.4 x 10^{-10} s^{-1}), while that for the heating peaks in the middle troposphere (with a value of ~3.1°K day^{-1}). Furthermore, the forcing is constant throughout each SWM simulation, having no temporal variability.

Given the above large collection of SWM simulations, the challenge is to isolate those simulations (i.e, forcing locations and forcing mechanisms: heating or vorticity) that are most relevant to understanding what drives a particular phenomenon of interest. We do that by identifying those forcing locations for which the response projects most strongly on our phenomenon of interest – our observed target anomaly pattern such as the PNA-like pattern. Our approach (described in detail in the Appendix), does this by first identifying (via an empirical orthogonal function expansion) the leading modes of variability across the SWM responses that resemble the target anomaly pattern, thereby effectively filtering out solutions that have no impact in the region of interest. We then isolate the important forcing locations associated with just those leading modes. We refer to those identified forcing locations as a "forcing sensitivity map", which can be mathematically expressed as a vector ($\vec{s}$) in which longitude and latitude are combined into a single dimension.

While the above sensitivity map provides insights into what may be the most relevant forcing regions for a particular target anomaly, we also provide various estimates of the actual forcings based on MERRA-2, the idea being that the most likely forcing of a particular observed circulation anomaly of interest (e.g., the PNA) occurs where the actual forcing overlaps with a region of large sensitivity as determined from the SWM experiments. In the case of vorticity, we

Accepted for publication in *Journal of Climate.* DOI 10.1175/JCLI-D-23-0696.1.

examine (from MERRA-2) the effective Rossby wave sources (RWSs) as defined by Sardeshmukh and Hoskins (1988). The leading RWS term is typically

$$-\nabla \cdot \left(V_\chi'(\bar{\zeta} + f)\right) = -(\bar{\zeta} + f)\nabla \cdot V_\chi' - V_\chi' \cdot \nabla(\bar{\zeta} + f). \quad (1)$$

where $\zeta = \nabla^2\psi$ is the vorticity, ψ is the stream function, and the subscripts ψ and χ denote the rotational and divergent components of the flow. For the results shown in Section 3.c.1, the overbar and prime denote a climatological La Niña mean and deviation from that mean, respectively. The two terms on the right-hand side of (1) are referred to as the "stretching" and advection terms, respectively. Here, we interpret the anomalous divergent flow (V_χ') as an "external" forcing, e.g., the divergence/convergence (stretching term) or the outflow/inflow (advection term) associated with the MJO.

In addition to the above linear sources of vorticity forcing, we also examine the nonlinear transient eddy flux convergence as defined in Ting and Yu (1998). This can be written in simplified form as (Wang and Ting 1999; DeAngelis et al. 2023):

$$\mathrm{TF}_{\mathrm{vor}} = -\nabla \cdot \overline{\mathbf{V}'\zeta'}, \quad (2)$$

where **V** is the horizontal wind vector. Here (Section 3.c.2), the overbar denotes a 7-day mean and primes are 6-hourly deviations from that mean. This vorticity forcing, which is typically associated with weather disturbances, has been shown to be an important forcing of stationary Rossby waves in the northern middle latitudes (e.g., Schubert et al. 2011, DeAngelis et al. 2023), and is computed from MERRA-2 6-hourly data. In order to better isolate the broader aspects of the transient vorticity forcing we apply an inverse Laplacian operator to that field. This acts as a natural spatial filter for what is typically a spatially noisy field (e.g., Schubert et al. 2011). We also examine estimates of the observed heating anomalies (these are based on MERRA-2, as described in DeAngelis et al. 2023).

Regarding our use of the SWM, it is important to emphasize that we do not rely on it to reproduce the detailed time evolution of the key circulation anomalies of interest. That is

Accepted for publication in *Journal of Climate.* DOI 10.1175/JCLI-D-23-0696.1.

obtained from our AGCM replay simulations. Besides the limitations of coarse vertical and horizontal resolution, and employing idealized fixed forcing functions, the SWM is by design highly damped and therefore does not allow for the development of transient eddy feedbacks – it only represents the direct response to a given forcing (Ting and Yu 1998). Nevertheless, we shall see that the SWM serves (via the sensitivity maps) an important purpose in helping interpret our replay results regarding those forcing locations and mechanisms most likely to be responsible for generating the responses of interest.

c. The GEOS S2S V2 model forecasts

We examine (in Section 3d) the results of a series of near-real-time subseasonal forecasts made with the GEOS S2S V2 coupled model (Molod et al. 2020). The components of the model of most relevance here are the GEOS atmospheric general circulation model [Molod et al., 2015; Rienecker et al., 2008], the Catchment land surface model [Koster et al., 2000], and the Modular Ocean Model-5 (MOM5) ocean general circulation model [Griffies et al., 2005; Griffies, 2012]. The AGCM component was run at ~0.5° spatial resolution with 72 hybrid sigma/pressure levels, while MOM5 was run at ~0.5° with 40 layers down to 4500 m depth.

A set of subseasonal retrospective forecasts were performed (to establish a climatology) with the GEOS S2S V2 model for the 17-year period from 1999–2015, following the protocol of NOAA's Subseasonal Experiment (SubX) project (Pegion et al., 2019). Initial conditions for the ocean were produced from a series of 5-day coupled ocean data assimilation runs, with the atmospheric conditions coming from MERRA-2. The retrospective forecasts were initialized every 5 days for a total of 73 start dates per year, with four ensemble members per start date. Near real time forecasts (which begin in 2017) are treated the same way, but are initialized from the GEOS-S2S-2 near-real-time weakly coupled atmosphere-ocean data assimilation system. Further details about the forecast procedure and initial conditions can be found in Molod et al. (2020). We examine in Section 3d forecasts that were issued for the period just prior to the development of the California floods.

Accepted for publication in *Journal of Climate.* DOI 10.1175/JCLI-D-23-0696.1.

3. Results

a. Background

Figure 1 shows that the California flooding occurred under La Niña conditions, with cold SST anomalies spanning much of the eastern tropical Pacific. Since all of our AGCM simulations are forced with observed SST we can expect to see some impact on the circulation that is typical of a response to the La Niña SST (e.g., Goss et al. 2018). We shall see that this is especially true for our NORPL runs for which the SSTs are the only source of external forcing. While much of the extratropical North Pacific had positive SST anomalies exceeding 1°C it is unlikely that these played a direct role in forcing the event (the so-called warm blob was already present since at least the spring of 2022, Chen et al. 2023) though any impact of those SSTs would again be included in all our AGCM runs. Figure 1 also outlines in red our two main replay regions (RPL_TR, RPL_WNP). The blue box outlines the region for our short duration replay runs (NORPL_IND).

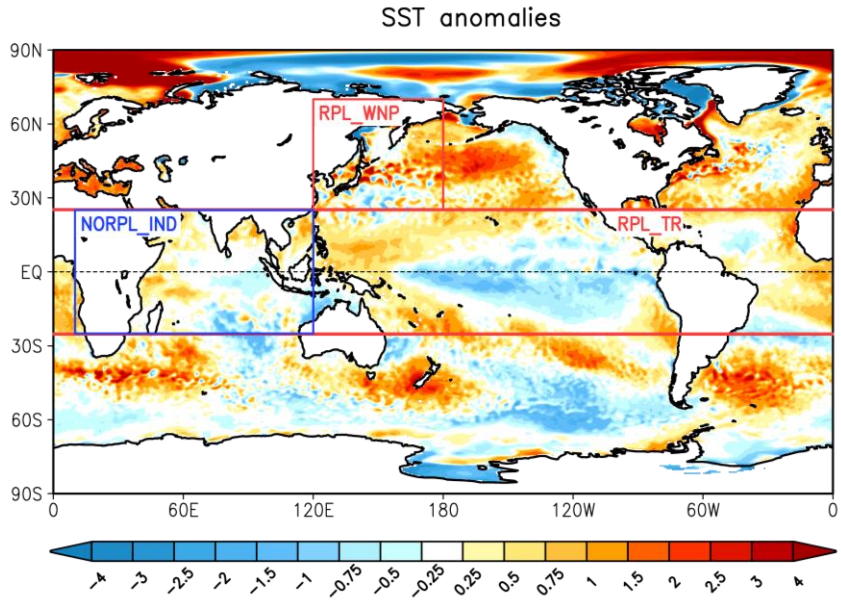

Figure 1: The SST anomalies(°C) averaged for the period 12/27/22 – 1/15/23, with superimposed red boxes outlining the two main replay regions (RPL_TR, RPL_WNP). The blue box indicates the short duration replay region centered on the Indian Ocean (NORPL_IND). See Table 1 for details.

Accepted for publication in *Journal of Climate.* DOI 10.1175/JCLI-D-23-0696.1.

Figure 2a shows the MERRA-2 precipitation anomalies averaged for the period 27 Dec 2022 to 15 Jan 2023[6]. For convenience we shall hereafter refer to the red box in Fig. 2a (35°N-45°N, 120°W-130°W) as the flood region, recognizing that it contains both land and ocean points. As discussed in the Introduction, the near record amount of precipitation that fell over California was associated with a series of narrow bands of moisture (ARs) entering the west coast from the North Pacific. This is reflected in the time series of the precipitation in the flood region (Figure 2b), which is characterized by a number of peaks between about December 27 and January 15: a period bracketed by vertical solid lines in Fig. 2b and hereafter referred to as the "flood period".

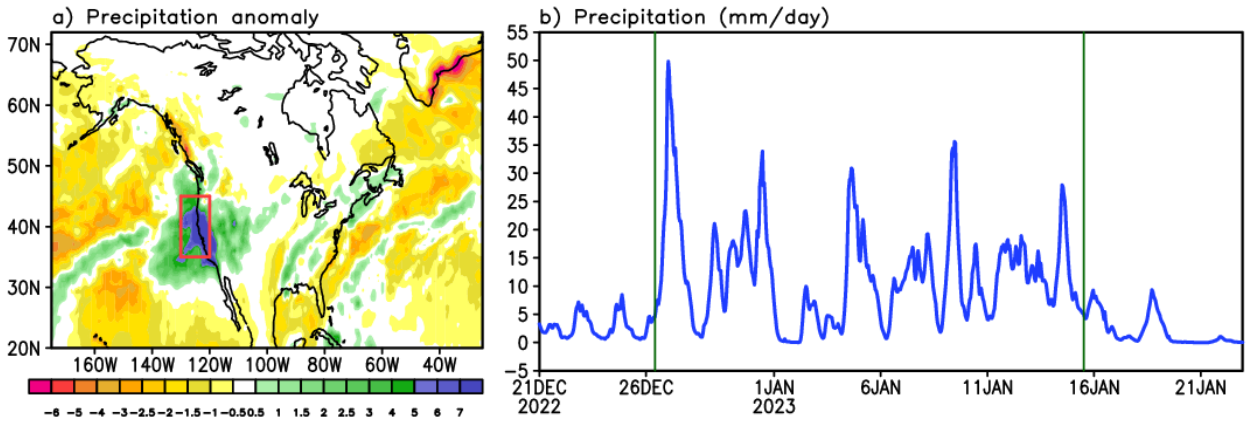

Figure 2: a. The MERRA-2 corrected precipitation anomalies (mm day^{-1}) averaged for the flood period 12/27/22 – 1/15/23. (Over continents, the corrected MERRA-2 precipitation data effectively represent rain gauge measurements.) The red box indicates our region of interest designated in the text as the flood region (35°N-45°N, 120°W-130°W). b. Time series of the daily precipitation (mm day^{-1}) averaged over the flood region. The solid vertical lines delimit the flood period considered in this paper (December 27 and January 15).

b. Model Simulations of the time mean flood period anomalies

We begin our analysis of the AGCM results with an overview of how well the different simulations (NORPL, RPL_TR, RPL_WNP) reproduced the observed (MERRA-2) extreme precipitation in the flood region during the flood period (12/27/22 – 1/15/23). Figure 3 is a scatterplot of the flood period precipitation anomalies for the flood region versus the associated

[6] Note that MERRA-2 precipitation is observationally corrected (Reichle et al. 2017).

Accepted for publication in *Journal of Climate*. DOI 10.1175/JCLI-D-23-0696.1.

850hPa magnitude of the moisture flux anomalies averaged along the west coast for MERRA-2 and all 45 ensemble members of the above-mentioned simulations. The scatter displays a strong linear relationship consistent with enhanced low-level moisture influx leading to an increase in precipitation. The MERRA-2 results are at the far end of the scatter of the model results and, as such, represent the most extreme values the AGCM is capable of producing when run in replay mode. The NORPL ensemble mean precipitation anomaly is essentially zero, and even the most extreme of the individual NORPL ensemble members show an anomaly only about half of that observed. RPL_TR produces an ensemble mean that is 42% of the MERRA-2 precipitation anomaly, and a few ensemble members do produce precipitation anomalies comparable to the observed. RPL_WNP approaches the MERRA-2 precipitation anomaly with even more ensemble members; its ensemble mean anomaly is 65% of that for MERRA-2. Also noteworthy is that the intra-ensemble scatter is larger for RPL_TR than for RPL_WNP. We shall come back to these results in Section 3c where we outline the sequence of events and underlying forcing regions that explain the differences in scatter and why both RPL_TR and RPL_WNP (but not NORPL) produce at least a few ensemble members with precipitation as extreme as the observed.

Accepted for publication in *Journal of Climate.* DOI 10.1175/JCLI-D-23-0696.1.

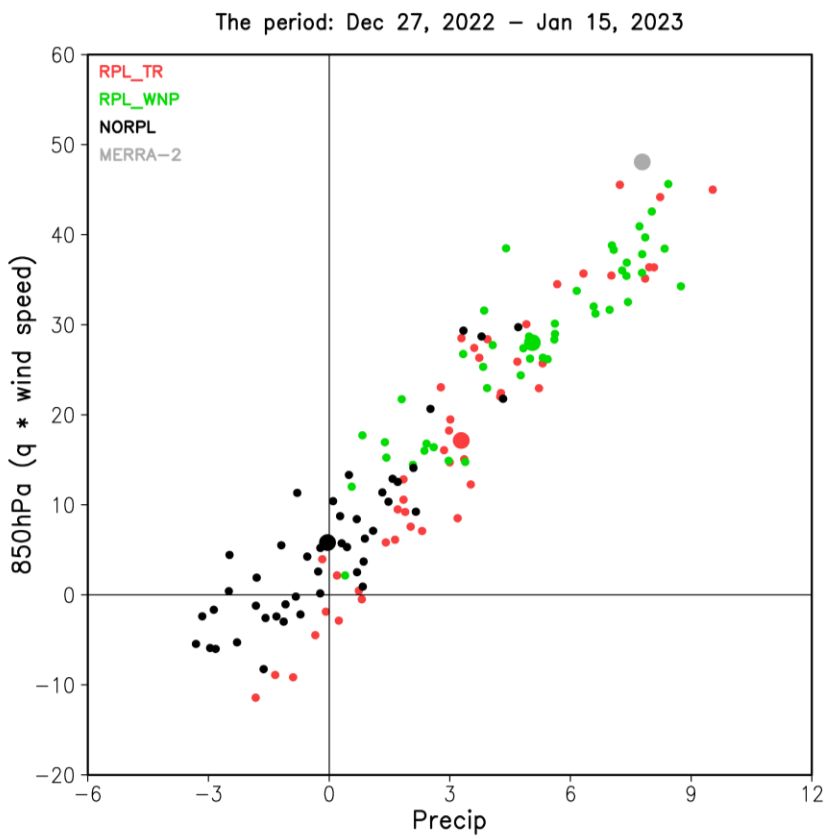

Figure 3: Scatterplot of the precipitation (mm day^{-1}) averaged over the flood region (35°N-45°N, 120°W-130°W) and the 850hPa magnitude of the moisture flux (g/kg m/s) averaged just off the west coast at (125°W, 35°N-45°N) for MERRA-2 and all the ensemble members (45) of the model runs (RPL_TR, RPL_WNP, NORPL). The large dots are the ensemble means and MERRA-2 results. The values are averages for the flood period (12/27/22-1/15/23).

Focusing now on the spatial patterns of the ensemble mean anomalies, Figure 4 shows the flood period time mean precipitation anomalies along with the superimposed 250 hPa height anomalies. Interestingly, with the exception of NORPL, all the model simulations and MERRA-2 show a pronounced positive PNA-like pattern, characterized by a large negative anomaly over the North Pacific (just off the coast) juxtaposed with a positive anomaly over North America. In fact, the daily observed PNA index was in a positive phase for much of the flood period[7]. Furthermore, the MERRA-2 main positive precipitation anomalies along the west coast (Fig. 4e)

[7] https://www.cpc.ncep.noaa.gov/products/precip/CWlink/pna/pna.shtml

Accepted for publication in *Journal of Climate.* DOI 10.1175/JCLI-D-23-0696.1.

are generally well reproduced by both RPL_TR (Fig. 4a) and RPL_WNP (Fig. 4c) though weaker than observed (see also Fig. 3). In contrast, NORPL (Fig. 4d) shows only very weak (less than 1 m day^{-1}) positive precipitation anomalies and those are situated too far to the north. Since RPL_TR does produce precipitation anomalies comparable to the observed for some ensemble members (Fig. 3), we show in Fig. 4b the average of just the 5 RPL_TR ensemble members with the largest precipitation anomalies in the flood region. This shows that indeed, those ensemble members produce precipitation and height anomalies closer to the observed in the Pacific/North American region (cf. Figs. 4a and b with 4e). A key feature of Fig. 4 is the strong spatial colocation of the flood region positive precipitation anomalies and the southeastern extent of the negative height anomaly, highlighting the tight coupling (evident in both MERRA-2 and the replay results) between the PNA and the ARs responsible for the flood region precipitation.

Here it is important to emphasize that a critical aspect of the positive PNA pattern shown for MERRA-2 in Fig. 4e is the extension of the negative anomaly eastward onto the coast, crucial for steering the storms onto the continent. In fact, the canonical positive PNA pattern puts the North Pacific negative anomaly somewhat off the coast[8] making it less effective in producing wet conditions over land. The canonical pattern also includes a negative lobe over the southeastern U.S., which we shall see only becomes evident during the second half of the flood period (e.g., Fig. 8h). We nevertheless for simplicity refer rather loosely to the sequence of anomalies in the North Pacific/North American region (e.g., Fig. 4e) as the positive PNA pattern, keeping in mind that they do differ in detail with the canonical pattern.

[8] https://www.cpc.ncep.noaa.gov/products/precip/CWlink/pna/pna.loading.shtml

Accepted for publication in *Journal of Climate.* DOI 10.1175/JCLI-D-23-0696.1.

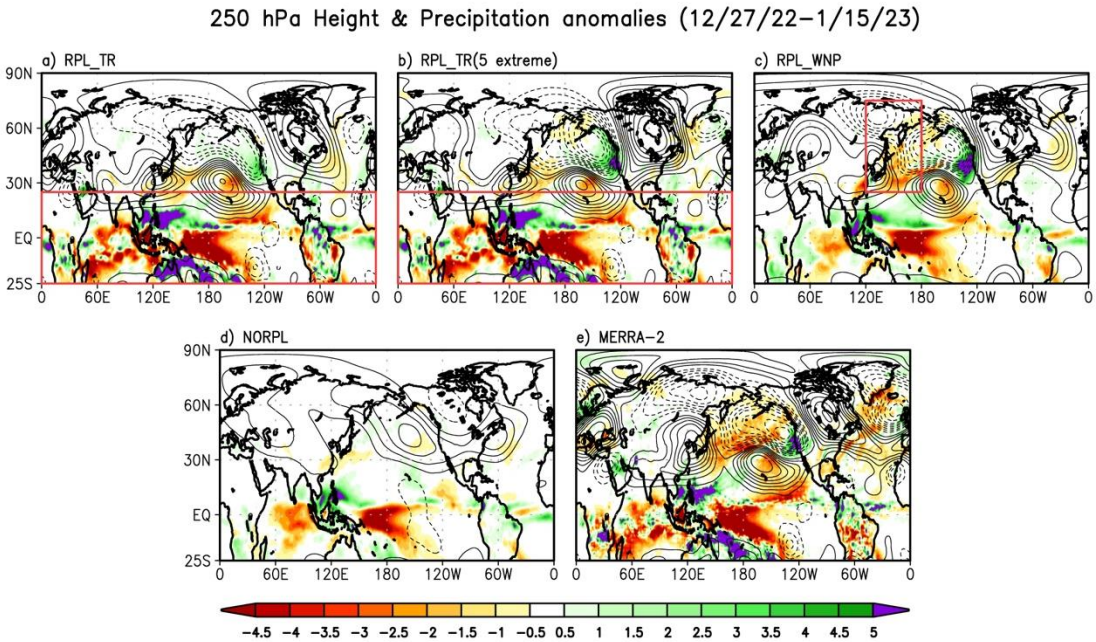

Figure 4: The ensemble average precipitation anomalies (mm day^{-1}, shaded) with superimposed 250 hPa height anomalies (meters, contoured) from the model experiments and MERRA-2 averaged for the flood period (12/27/22-1/15/23). The panels consist of, a) RPL_TR, b) RPL_TR averaged for only the 5 ensemble members with the largest precipitation anomalies over the flood region), c) RPL_WNP, d) NORPL, and e) MERRA-2. The height contours are drawn every 20 m, with negative contours dashed and zero omitted, up to a magnitude of 120 m, then every 30 m thereafter.

Looking more broadly at the precipitation anomalies, we see that both RPL_WNP and NORPL produce tropical anomalies that are overall similar to the observed/MERRA-2 (and of course by design similar to RPL_TR) anomalies, reflecting the strong control of the La Niña SST anomalies on the tropical precipitation. However, only NORPL produces the height anomalies over the PNA region (Fig. 4d) that one would expect as a canonical response to La Niña SST anomalies (e.g., Goss et al. 2018): anomalies that are essentially opposite to what actually occurred over the North Pacific. This indicates that the positive PNA seen in the observations developed not as a result of forcing from the tropical SST anomalies, but despite that forcing. Understanding how that happened is the subject of the next section.

Accepted for publication in *Journal of Climate.* DOI 10.1175/JCLI-D-23-0696.1.

c. Initiation and development of the event

Some clues to what drove the positive PNA can be gleaned from Figure 5, which shows the December through mid-January evolution of the 250 hPa height anomalies averaged between 30°N and 60°N for MERRA-2 and the model simulations. Immediately clear is that NORPL is again an outlier showing generally positive height anomalies in the central North Pacific throughout that time period (Fig. 5d). Focusing on MERRA-2 (Fig. 5e), two things stand out. First, starting in late December, generally negative anomalies occur just off the west coast (roughly 120°W) along with positive anomalies to the east of that linked to the development of the positive PNA. In fact, the day-to-day evolution of the height anomalies (not shown) shows that the positive PNA develops rather abruptly around December 25-26. Second, we see that the start of the positive PNA in late December is preceded by enhanced eastward propagating wave

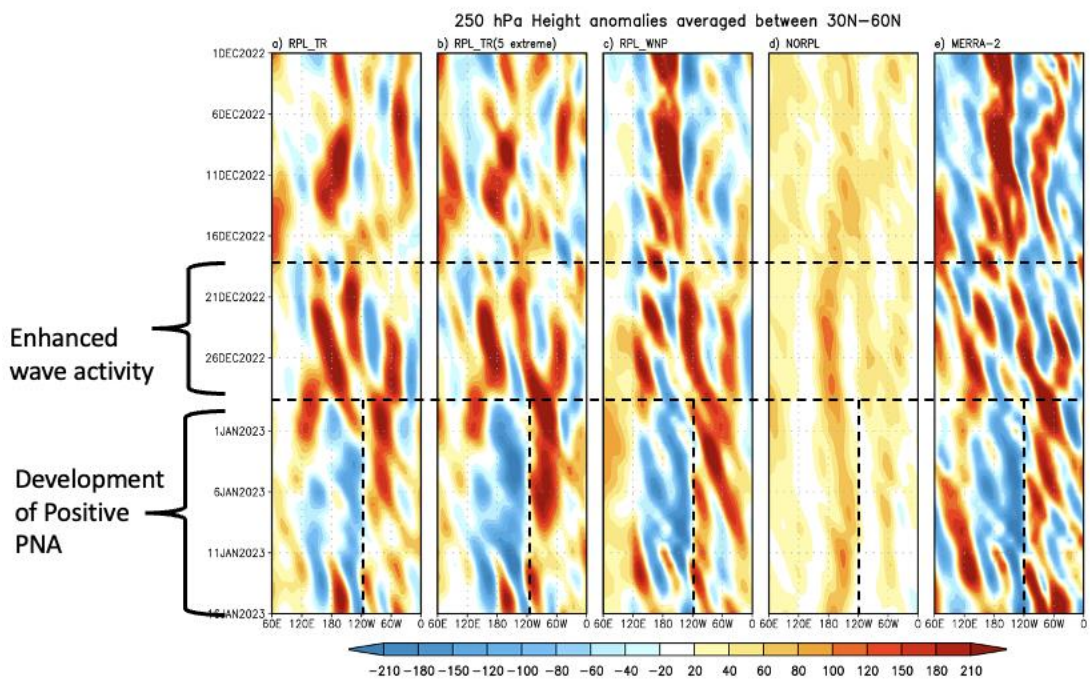

Figure 5: The longitude/time hovmöller plots of the ensemble mean 250hPa height anomalies (averaged between 30°N-60°N) from the model experiments and MERRA-2. The panels consist of, a) RPL_TR, b) RPL_TR averaged for the 5 ensemble members with the largest precipitation anomalies in the flood region, c) RPL_WNP, d) NORPL, and e) MERRA-2. The two horizontal dashed lines identify the beginning of the enhanced wave activity and the beginning of the mature phase of the positive PNA. The vertical dashed lines identify 120°W longitude. Units are meters.

Accepted for publication in *Journal of Climate.* DOI 10.1175/JCLI-D-23-0696.1.

activity starting in mid-December. This overall behavior is reproduced in RPL_TR, RPL_TR (5 extreme) and RPL_WNP (Figs. 5a-c), suggesting the enhanced wave activity may have played a role in initiating the development of the PNA.

In fact, a spatial map of that wave activity suggests that this is part of a wave train that is emanating from the Indian Ocean region (see Fig. 7a) – a wave train we shall refer to in the following as the Indian Ocean short wave or ISW. As we shall see next, the ISW appears to be critical to the eventual forcing of the positive PNA. As such, we will first determine what initiated the ISW (Section 3.c.1), and then determine how that led to the positive PNA (Section 3.c.2).

1) Initiation

To examine the development of the ISW, we begin by examining the results of replaying to MERRA-2 over a limited tropical region encompassing the Indian Ocean for the 10-day period Dec 14-23, 2022 (NORPL_IND, see Table 1). The motivation for this replay experiment is to further isolate (both spatially and temporally) the region responsible for the development of the ISW and hence, to the extent that leads to the development of the positive PNA (Section 3.c.2), the ultimate remote forcing region of the flooding. We theorize that the development of the ISW is related to the MJO which had, in mid-December, its active phase situated over the eastern Indian Ocean/Maritime continent[9]. Fig. 6 shows the daily evolution of the 250 hPa stream function (ψ) anomalies[10] during the replay period. An anticyclonic couplet centered on the equator over the Indian Ocean (Dec 14) is followed by the initiation of the ISW a few days later (Dec 16), which by Dec 22 resembles the mature observed ISW (Fig. 7a). The initial development (in particular the anticyclonic couplet) is consistent with the Rossby wave response that occurs on the trailing edge of the active phase of the MJO (e.g., Wang et al. 2016). We will come back to the key role of that anticyclonic couplet in forcing the ISW when discussing our SWM results below.

[9] http://www.bom.gov.au/climate/mjo/

[10] Here we compare with the NORPL results rather than computing anomalies, which would require computing a separate climatology for these replay runs. This should be sufficient for our purposes since our goal here is only to assess impacts.

Accepted for publication in *Journal of Climate.* DOI 10.1175/JCLI-D-23-0696.1.

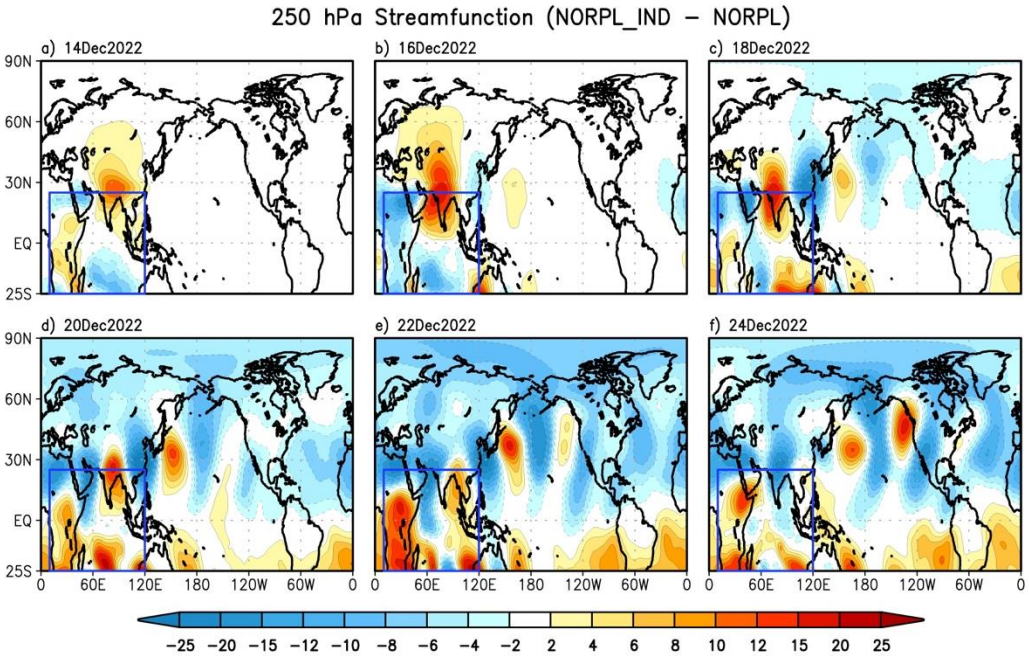

Figure 6: The daily evolution of the 250 hPa stream function anomalies (10^6 m^2s^{-1}, NORPL_IND –NORPL). NORPL_IND was replayed for the 10-day period 14 Dec to 23 Dec, 2022, in the area indicated by the blue box. The results are 45-member ensemble means.

We next employ the SWM simulations to further pinpoint the forcing region and forcing mechanism for the ISW (see Section 3b and the appendix for a description of our approach). Our choice of the base state for the SWM experiments is canonical December La Niña conditions given the presence of La Niña during December 2022; we wanted to employ a base state with a jet that resembles the 2022 conditions but does not include the anomalies of interest. (Comparing Figs S1a and b we see that the 2022 December East Asian/North Pacific jet is indeed rather similar to the canonical La Niña December jet.) Figure 7a shows our target ISW averaged here for Dec 21-23 (based on MERRA-2, and outlined by the black box). This is roughly the period when the ISW achieves its mature phase. Fig. 7b shows that we are able to reproduce the observed ISW quite well with the sum of the SWM responses to vorticity, with each scaled by the corresponding vorticity sensitivity value shown in Fig. 7c. The sensitivity map underscores the importance of the forcing that occurs along the southern flank of the jet. Forcing there (particularly positive vorticity west and south of India) appears to be the most efficient way to generate the ISW, which then develops and propagates within the jet wave guide.

Accepted for publication in *Journal of Climate.* DOI 10.1175/JCLI-D-23-0696.1.

The question then is whether there is any spatial overlap between the above sensitivity map and the actual forcing. Fig. 7d shows that we do find a substantial positive RWS in the North Pacific jet entrance region over the Middle East in mid-December (Dec 16-17). While this forcing is located at the northern edge of the most sensitive positive vorticity forcing region (Fig. 7c), we nevertheless believe it is most likely key to initiating the ISW. This forcing is associated almost entirely with the RWS stretching term (eq. 1), as a result of convergence in the presence of climatological positive absolute vorticity (not shown). Fig. S2 establishes the link between that convergence over the Middle East and the developing MJO based on MERRA-2. In particular, Fig. S2a links the outflow from the developing active phase of the MJO located over the Indian Ocean/Maritime Continent to the convergence over the Middle East. Figs. S2b and c provide evidence for a dynamical interpretation for the location of the convergence in terms of the anticyclonic circulation anomaly centered over India: the anticyclonic anomaly (the Northern Hemisphere component of the MJO-related anticyclonic couplet mentioned earlier) produces an acceleration of the jet, and thereby induces an anomalous transverse ageostrophic wind and convergence on the left flank of the jet's entrance region (e.g., Uccellini and Johnson 1991).

Finally, we note that a similar analysis based on the SWM heating experiments (Fig. S3) indicates that cooling in the Red Sea area along the southern flank of the jet is especially conducive to generating the ISW, but we find no evidence of a substantial cooling anomaly in that region in the observations, indicating heating anomalies did not play a direct role in forcing the ISW.

Accepted for publication in *Journal of Climate.* DOI 10.1175/JCLI-D-23-0696.1.

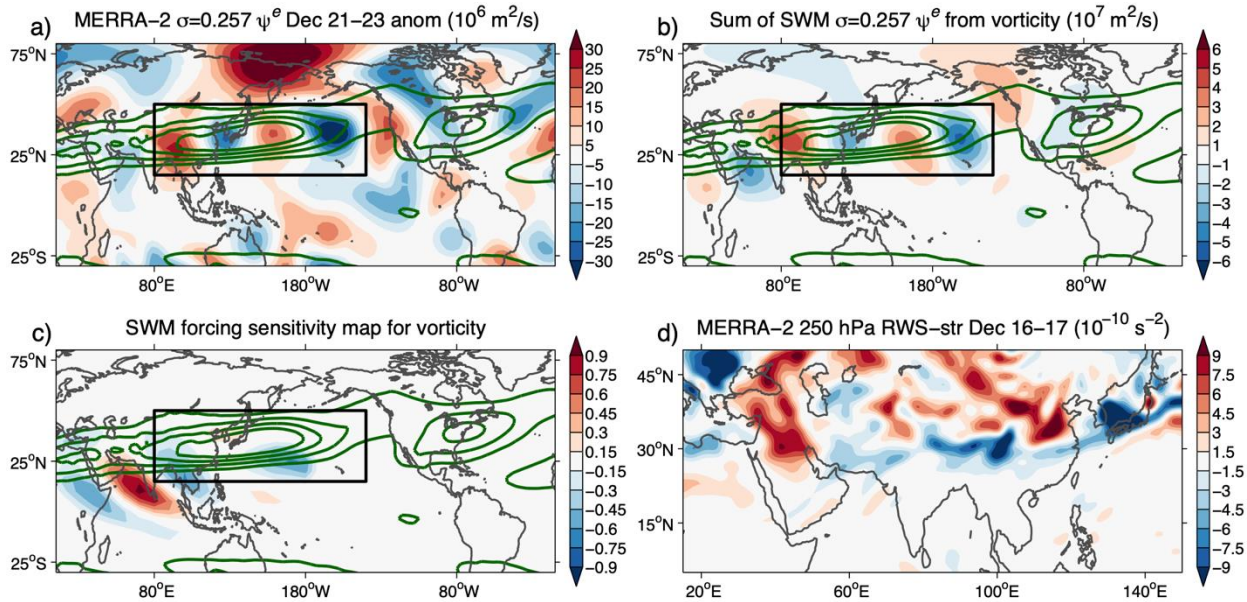

Figure 7: Results of the stationary wave model (SWM) simulations focusing on the Indian Ocean short wave (ISW) using a canonical December La Niña base state. a) The observed ISW eddy stream function (ψ^e, where the eddy is computed by subtracting the zonal mean) anomalies averaged for Dec 21-23 from MERRA-2, interpolated to sigma level (σ) 0.257 (10^6 m^2 s^{-1}). b) Reconstruction of the ISW (ψ^e at σ=0.257, 10^7 m^2 s^{-1}), computed by scaling the SWM response maps to vorticity forcing (each associated with a specific forcing location) by the forcing sensitivity at the corresponding forcing locations (shown in panel c) and then summing them. c) The sensitivity map ($\vec{s}$, see appendix) for vorticity forcing (shaded). d) The Rossby wave source (RWS, 10^{-10} s^{-2}) associated with the stretching term (first term on RHS of eq. 1) averaged for Dec 16-17 at 250 hPa, estimated from MERRA-2. In panels a-c, the contours are the upper tropospheric (σ=0.257) canonical December La Niña zonal wind based on MERRA-2 (contours every 10 m s^{-1} starting at 20 m s^{-1}), and the boxes outline the target region defined by the ISW in (a).

2) Development of the positive PNA

Turning now to the flood period, we first examine whether the NORPL_IND simulations (which, as we have seen, did produce the ISW) do indeed develop a positive PNA anomaly. Here we remind the reader that the 10-day replay period ended on Dec 23 (well before the flood period and development of the positive PNA) after which the simulations were free-running being forced only by the observed SST. We revert back to the NORPL configuration in order to isolate the relevant tropical forcing to that 10-day time period. As such, we are interested in determining if the free-running (NORPL) model, after being given the correct tropical forcing for a short time, can go on to produce the PNA on its own (Fig. 4). Fig. 8 shows the results

Accepted for publication in *Journal of Climate.* DOI 10.1175/JCLI-D-23-0696.1.

averaged separately for the first half of the flood period (12/27/22-1/5/23, top row) and the second half of the flood period (1/6/23-1/15/23, bottom row). As we shall see, these two periods have somewhat different PNA-like structures and potentially different forcing mechanisms. We refer to those as the early and late flood periods.

Focusing on the NORPL_IND results (Figs. 8b and f), we see that the 10-day replay does indeed generate a positive (though weak) ensemble mean positive PNA-like anomaly after the replay period, characterized by a positive anomaly over western North America and a negative anomaly in the central North Pacific that amplifies and expands eastward toward the west coast during the course of the flood period. The associated NORPL_IND positive precipitation anomalies (Figs. 8b and f) are also weak and primarily off the coast, reflecting again the strong link with the (in this case) weak and westward displaced negative height anomalies. Focusing on the average of just the five NORPL_IND ensemble members with the most extreme precipitation anomalies in the flood region (Figs. 8c and g) we see that the PNA anomaly, while still weaker than observed during the early flood period (cf. Figs. 8c and d), approaches (in amplitude, structure, and location) that of the observations during the late period (cf. Figs. 8g and h). The associated precipitation anomalies (Figs. 8c and g) now extend onto the coast and are much more like the observed in amplitude, though still displaced somewhat to the north compared with the observations. This reflects the sensitivity of the location of the precipitation anomalies to rather small (from a global perspective) displacements of the key negative height anomaly just off the coast. Comparing the above with the NORPL results (Figs. 8a and e), we see that the SST forcing tends to produce essentially the opposite circulation anomalies in the PNA region, and very weak (less than 1 mm day^{-1}) positive precipitation anomalies along the coast that are well north of the flood region.

In summary, while the PNA anomaly (and associated precipitation anomalies) generated in NORPL_IND are not an exact reproduction of the observed, the above results are nevertheless highly suggestive of the ISW (and its probable MJO source) being a key factor in generating the positive PNA and associated flood region precipitation anomalies.

Accepted for publication in *Journal of Climate.* DOI 10.1175/JCLI-D-23-0696.1.

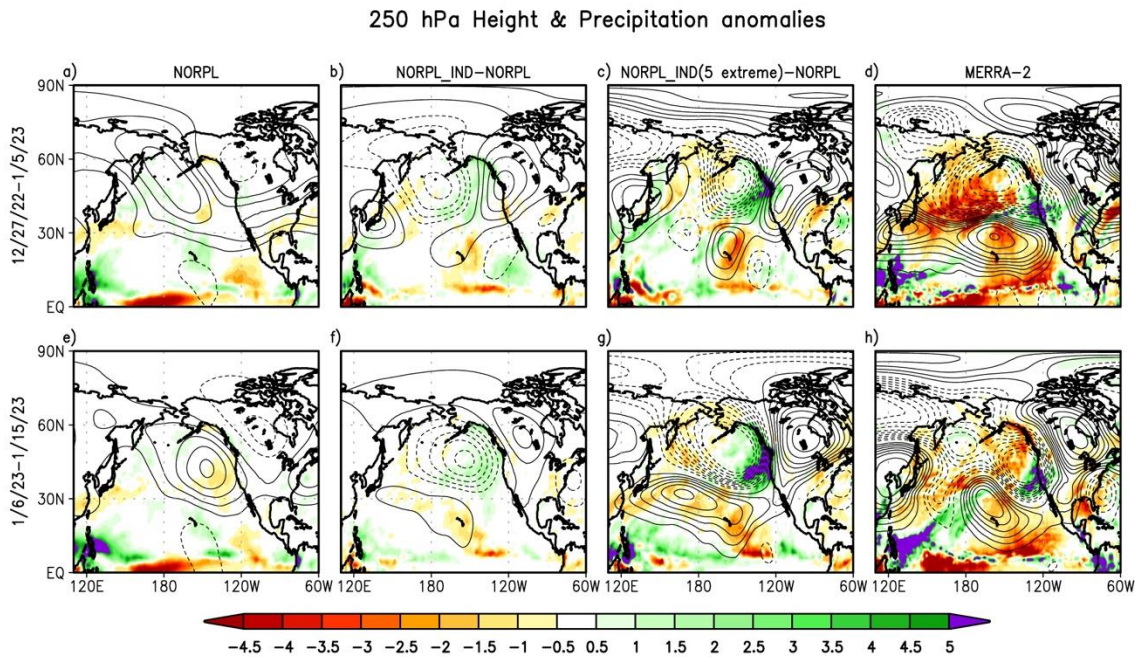

Figure 8: The 250 hPa height anomalies (contoured, meters) and precipitation anomalies (shaded, mm day^{-1}) during the flood period. Top panels are for the first half of the flood period (12/27/22-1/5/23), and the bottom panels are for the second half of the flood period (1/6/23-1/15-23). From left to right the results are for NORPL, NORPL_IND – NORPL, NORPL_IND (5 extreme)-NORPL and MERRA-2. The height contours are drawn every 20 m, with negative contours dashed and zero omitted, up to a magnitude of 120 m, then every 30 m thereafter.

Before turning to the SWM results to further pinpoint the nature and location of the forcing of the PNA, we note one interesting difference in the observed PNA between the early and late periods (cf. Figs. 8d and h). The early period PNA has a clear north/south dipole structure in the North Pacific, while the late period PNA has a much more (southwest to northeast) wave-like structure (something reproduced in both our RPL_TR and RPL_WNP results, not shown) - the implication being that the early and late period PNA may have had somewhat different forcing. With this in mind, we next focus our SWM analysis on the early period (most relevant for the initiation of the PNA).

We begin with a focus on the role of vorticity forcing. Fig. 9a shows the early period PNA outlined by the box defining the target region for our SWM analysis. Fig. 9b illustrates that we are able to largely reproduce the early period PNA as the sum of the SWM responses to vorticity, each scaled by the corresponding vorticity sensitivity value (Fig. 9c), including the north/south

Accepted for publication in *Journal of Climate.* DOI 10.1175/JCLI-D-23-0696.1.

dipole structure that distinguishes it from the late period PNA. The sensitivity map underscores the importance of the vorticity forcing that occurs along the southern flank of the jet. Positive values over southeast Asia and the southern flank of the jet exit region appear to be important, while negative vorticity forcing east of Hawaii appears to be especially effective in producing a positive PNA. Fig. 9d shows the transient vorticity forcing (eq. 2) during the week just before the PNA develops (Dec 21-27). The generally positive values along the equatorward flank of the jet (especially at the jet exit), appear to have sufficient overlap with the positive sensitivity values (Fig. 9c) to provide forcing for the positive PNA. We interpret the transient vorticity forcing as linked to the ISW which achieves its largest amplitude within the North Pacific jet wave guide during that time.

While the vorticity forcing along the southern flank of the jet tied to the ISW appears to be key to the development of the positive PNA in late December, it is unclear whether MJO heating may have also played a more direct role (beyond initiating the ISW) in supporting the development of the PNA. To address this, Figure S4 shows the evolution of the MJO-related OLR anomalies focusing on the following three periods: December 21-26 (the time period during which the MJO achieved its maximum amplitude[9]), December 27-January 5 (the early flood period when the positive PNA is already well established), and January 6-15 (the late flood period, when the PNA has evolved into a more wave-like structure). Fig. S4a shows that during December 21-26, the main MJO-related heating anomaly (as reflected in negative OLR values), while relatively strong, is situated south of the equator just to the northwest of Australia. This, together with the occurrence of easterlies north of the equator (not shown), would tend to inhibit any response to that heating from propagating northward into the PNA region. This is supported by the SWM sensitivity map to heating which shows little if any sensitivity to heating anywhere in the tropical Pacific associated with the early flood period PNA pattern (Fig. S4d). Focusing now on the OLR anomalies during the early flood period (Fig. S4b), we see that the negative anomaly northwest of Australia has weakened considerably, while another relatively weak negative anomaly occurs over Indonesia. Our SWM sensitivity maps for heating for the late flood period PNA[11] pattern (Fig. S5c) again indicates little sensitivity to heating northwest of

[11] Our choice of the base state for the SWM experiments for the late period is the January canonical El Niño conditions (rather than the canonical La Niña conditions used for the early period). This choice is

Accepted for publication in *Journal of Climate.* DOI 10.1175/JCLI-D-23-0696.1.

Australia, but it does show a weak sensitivity to heating just to the northeast of Indonesia, suggesting a possible impact on the late period PNA from the heating there.

Finally, Fig. S5c shows that the greatest sensitivity to heating actually occurs in a region just northwest of Hawaii. This coincides with a region of positive heating anomalies (Fig. S5d) and appears to play a much greater role than tropical heating in contributing to the longevity and the overall southwest/northeast structure of the late period PNA (Fig. S5b). That positive heating anomaly is, in fact, associated with the enhanced storminess/ precipitation that was facilitated by the early flood period PNA, reflecting what appears to be a feedback on the PNA.

The main results of this section are summarized in Figure 10 as follows. Starting in mid-December convergence linked to the outflow from the MJO (1) resulted in a vorticity source (2) just west of 60°E (the exact location being tied dynamically to the MJO's impact on the North Pacific jet, Fig. S2). That vorticity source generated a Rossby wave (3, the ISW) that propagated within the jet wave guide from the northern Indian Ocean into the North Pacific reaching maximum amplitude on December 21-23. The ISW in turn generated a vorticity source (4, transient eddy vorticity flux convergence) along the southern flank of the jet exit region thereby forcing a positive PNA on about December 25-26 (5). Finally, a key feature of the positive PNA (not illustrated in Fig. 10) was the fact that it persisted from late December into mid-January thereby facilitating the development and steering of the family of ARs that hit the California coast over the course of almost three weeks. Our results (Fig. S5) show this persistence of the positive PNA is at least in part the result of a feedback to the heating (precipitation) just west of Hawaii produced by those ARs.

based on the fact that the PNA at that time evolves within the more extended (elongated) jet environment produced by the early period positive PNA (see Figs S1c and d compare the January canonical El Niño and 2023 January North Pacific jets).

Accepted for publication in *Journal of Climate.* DOI 10.1175/JCLI-D-23-0696.1.

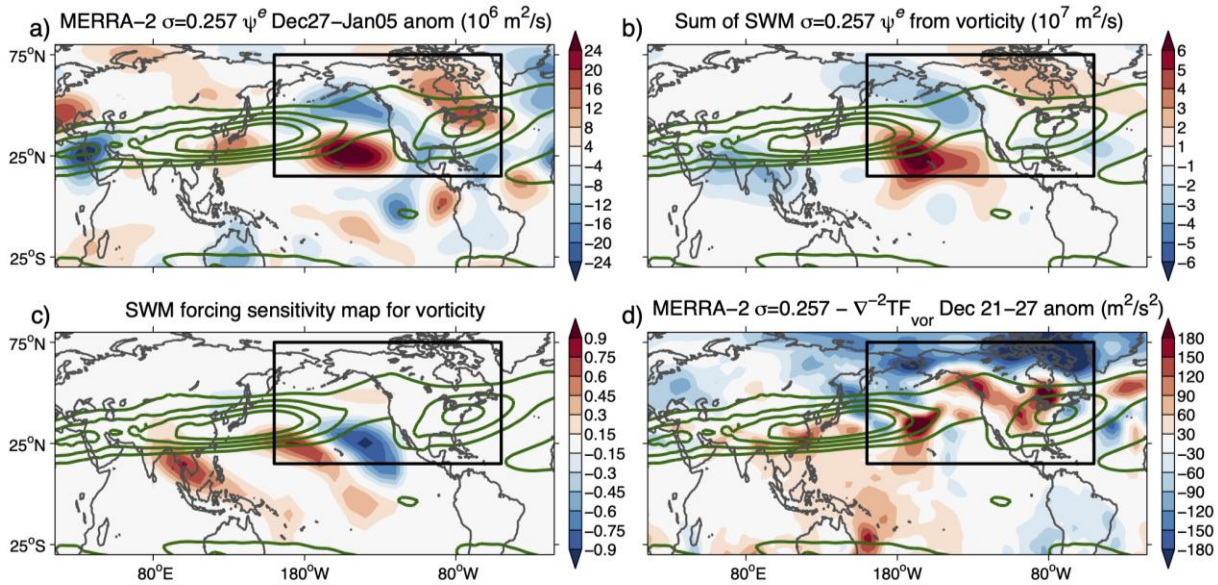

Figure 9: Results of the stationary wave model (SWM) simulations focusing on the early period (Dec 27-Jan 5) PNA with a canonical December La Niña base state. a) The observed PNA ψ^e anomalies averaged for the early period from MERRA-2, interpolated to σ=0.257 (10^6 m^2 s^{-1}). b) Reconstruction of the early period PNA (ψ^e at σ=0.257, 10^7 m^2 s^{-1}), computed by scaling the SWM response maps to vorticity forcing (each associated with a specific forcing location) by the forcing sensitivity at the corresponding forcing locations (shown in panel c) and then summing them. c) The sensitivity map ($\vec{s}$, see appendix) for vorticity forcing (shaded). d) The transient vorticity forcing (negative of the inverse Laplacian, see text) for the period Dec 21-27 based on MERRA-2, interpolated to σ=0.257 (m^2 s^{-2}). In all panels, the contours are the upper tropospheric (σ=0.257) canonical December La Niña zonal wind based on MERRA-2 (contours every 10 m s^{-1} starting at 20 m s^{-1}), and the boxes outline the target region defined by the PNA in (a).

Accepted for publication in *Journal of Climate.* DOI 10.1175/JCLI-D-23-0696.1.

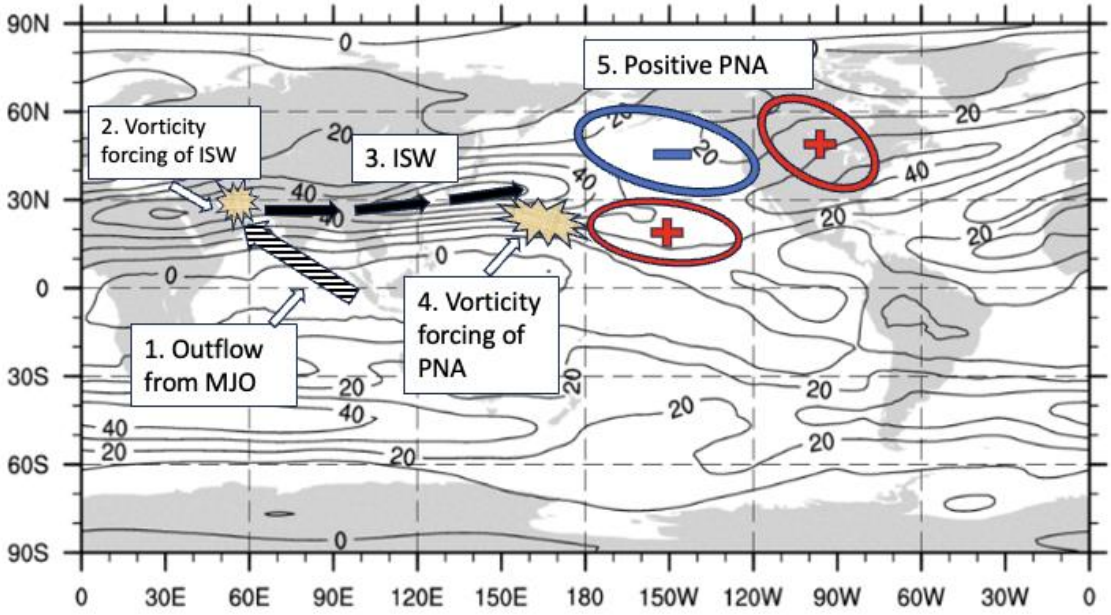

Figure 10: A schematic summarizing the sequence of events that led to the development of a positive PNA in late December 2022. The contours are the Dec/Jan 2022/23 mean zonal wind at 250 hPa from MERRA-2 (m s^{-1}).

The above schematic provides insight into how to interpret the results of the RPL_TR and RPL_WNP simulations (e.g., Fig. 3), with both producing the extreme flood region precipitation, but RPL_WNP producing an ensemble mean closer to the observed (and with less intra-ensemble spread). From a predictability perspective those two replay areas constrain different processes in the sequence of events leading to the positive PNA (and the resulting extreme precipitation over California), with RPL_TR constraining the earliest events (the vorticity forcing of the ISW linked to the MJO), and RPL_WNP constraining events much closer to the initiation of the PNA (the mature ISW and associated vorticity forcing in the jet exit region). That there is considerable intra-ensemble scatter (uncertainty) in the flood region precipitation even for the RPL_WNP simulations is likely a reflection of the underlying barotropic instability of the North Pacific jet, with PNA-like structures being particularly susceptible to growth (Simmons et al. 1983).

Accepted for publication in *Journal of Climate.* DOI 10.1175/JCLI-D-23-0696.1.

d. Forecast skill at sub-seasonal time scales

Our AGCM replay and SWM results indicate that there are two critical junctures in the sequence of events leading to the positive PNA (see Fig. 10). The first is in mid-December (16-17th) with the initiation of the ISW as a result of vorticity forcing linked to the outflow from the MJO, and the second is in late December with the initiation of the positive PNA (Dec 25- 26th) as a result of vorticity forcing in the jet exit region tied to the mature ISW. With that in mind, we next examine forecasts produced with the GEOS S2S model as part of SubX (see section 2c) at various forecast leads to document the lead times at which a state-of-the-art coupled forecast system is able to predict the PNA and precipitation extremes.

Figure 11 shows the 4-member ensemble mean forecasts initialized every 5 days beginning in mid-December (Dec 12, 17, 22, and 27). Figs. 11a and b show that the precipitation in the flood region and the 250 hPa height anomalies are reasonably well forecast for the December 22 initialization but not before that, though there is some signature of the positive PNA even for the Dec 17 initialization (though shifted to the west). As such, our first critical juncture (the initiation of the ISW in mid-December) appears to be the defining point separating skillful and unskillful forecasts. In fact, the more skillful December 22 forecasts were initialized at a time in which the ISW had already achieved a mature state, so those forecasts were presumably more skillful in predicting the associated vorticity forcing (in the jet exit region) of the PNA. What is most surprising is that the forecasts initialized December 27 are less skillful than the December 22 forecasts, failing to adequately capture both the precipitation and 250 hPa height anomalies. These forecasts are initialized at a time early in the PNA's development - so presumably in the midst of considerable sensitivity to the initial conditions associated with the barotropic instability of the jet (Simmons et al. 1983; Schubert et al. 2001), though exactly why that should lead to less skillful forecasts than those initialized 5 days earlier is unclear.

Fig. 11c quantifies the differences in skill of predicting the PNA, showing that the Dec 17 forecast loses skill after about one week, and that the Dec 22 forecasts remain skillful for about 3 weeks, while the Dec 27 forecasts lose skill quite rapidly after about 2 weeks. Although it is possible that these results reflect sampling error (only 4 ensemble members make up each forecast), a closer examination of the individual ensemble members and separating the

Accepted for publication in *Journal of Climate.* DOI 10.1175/JCLI-D-23-0696.1.

verification times into the early and late flood periods (not shown) shows a consistency among the ensemble members suggestive of a real difference in skill. Further work is required to understand this result. In any event, a two to three-week skillful forecast of the precipitation in the flood region is rather remarkable given the chain of events involving internal atmospheric variability outlined above.

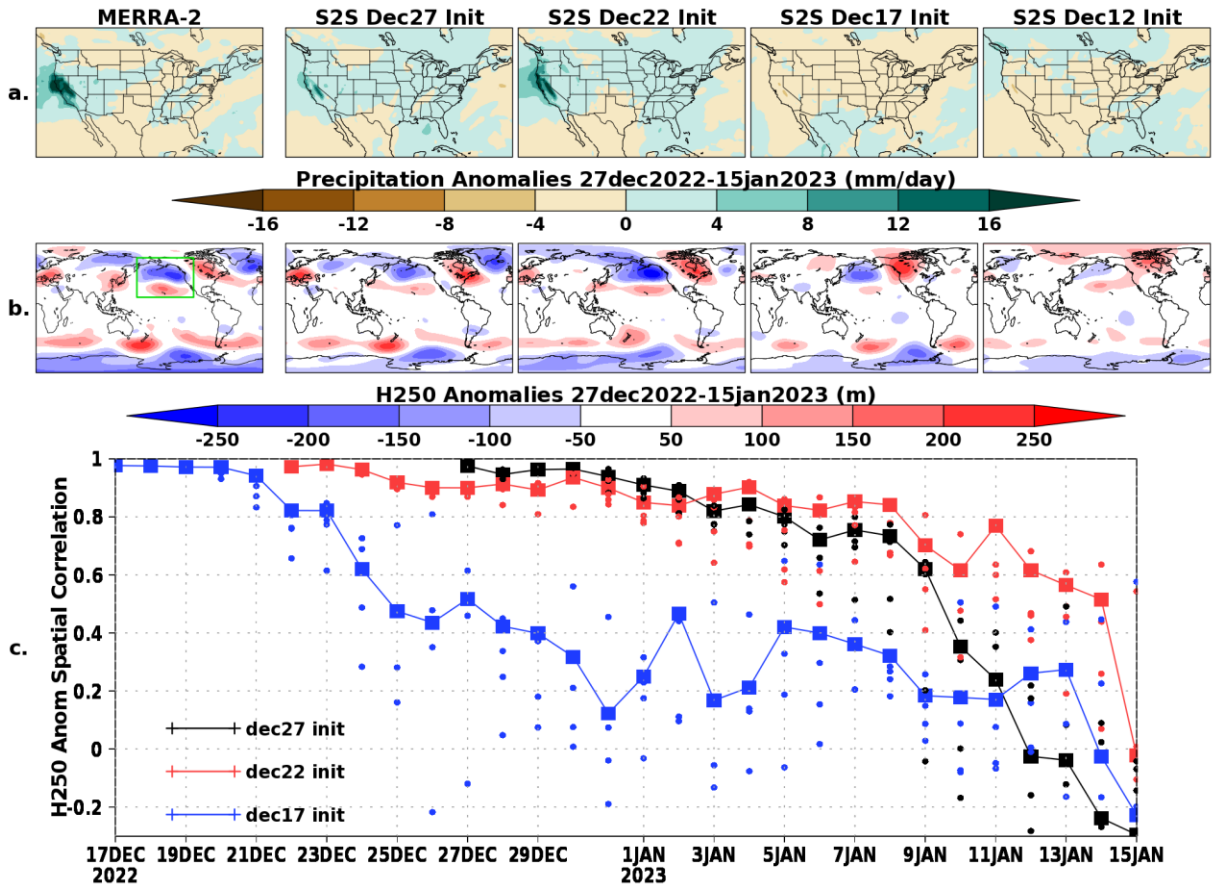

Figure 11: Hindcasts of a) the precipitation (mm day^{-1}) and b) the 250 hPa height anomalies (m) averaged for the period 27 December to 15 January 2023, produced by the GEOS S2S V2 coupled model for selected initialization dates (Dec 12, 17, 22 and 27). Left panels are for MERRA-2, followed by the 4-member ensemble means. c) The 250 hPa height anomaly spatial correlations with MERRA-2 for the Dec 17, Dec 22 and Dec 27 initialization dates as a function of forecast time. Large dots are the ensemble means and the small dots are the 4 individual ensemble members. The spatial correlation is computed over the green box in b). The climatology is 1999-2021.

Finally, we note that these results are consistent with the recent findings of DeFlorio et al (2023). They examined the skill of experimental seasonal and subseasonal forecasts in predicting the

Accepted for publication in *Journal of Climate*. DOI 10.1175/JCLI-D-23-0696.1.

regime shift from dry to wet conditions associated with the 2022/23 California flood. They found that the seasonal forecasts underpredicted the above normal precipitation across Northern and Central California which they attributed to an overreliance on La Niña. On the other hand, they found that the subseasonal forecasts did capture the shift from dry to wet conditions in late December 2022 at 2-3 week lead times. They pointed to a likely role of the MJO which was in a phase that historically tilts the odds towards increased AR activity over California.

4. Discussion and Conclusions

We examined here the underlying causes and predictability of the near record precipitation that fell on the west coast of the U.S. during the period December 27-January 15, 2023. The rainfall was associated with an unusually active eastern North Pacific storm track and associated family of atmospheric rivers that funneled moisture into the continent, with California being hit especially hard. The unusual storminess occurred within a persistent large-scale cyclonic circulation anomaly anchored just off the coast as part of a positive PNA anomaly pattern that spanned the North Pacific and North America during much of that time. Here we remind the reader that this pattern differs from the canonical PNA which places the negative anomaly further to the west making it less effective in steering storms onto the coast. It is likely such differences have less to do with the forcing of the PNA and more to do with the underlying instability of the North Pacific jet as discussed below.

A key question we addressed in trying to explain the cause of the extraordinary rainfall is what forced the persistent positive PNA which played a key role in steering and facilitating the development of the family of ARs. We show that SST anomalies did not play a direct role. In fact, the existing La Nina SST anomalies would only encourage circulation anomalies essentially opposite to those observed in the PNA region. This explains the lack of skill of seasonal outlooks which rely heavily on the response to SST at such long leads. It is consistent with the PNA being a largely internal mode of atmospheric variability (Straus et al. 2002). Our replay simulations, in which we constrained the model to remain close to MERRA-2 over selected regions of the globe (the tropics and western North Pacific), combined with more idealized SWM experiments, suggest that the development of the positive PNA was indeed the result of a

Accepted for publication in *Journal of Climate.* DOI 10.1175/JCLI-D-23-0696.1.

sequence of events and forcings involving internal atmospheric variability. In particular, we provide evidence that the event was initiated in mid-December by a Rossby wave (referred to as the Indian Ocean short wave or ISW) which propagated within the jet wave guide from the northern Indian Ocean into the North Pacific as a result of vorticity forcing linked to the developing MJO. The ISW in turn generated a vorticity source along the southern flank of the North Pacific jet exit region thereby forcing a positive PNA on about December 25-26. Furthermore, the fact that the positive PNA persisted almost three weeks (into mid-January) was at least in part the result of a feedback to the heating in the North Pacific (just west of Hawaii) produced by the ARs.

Considering that many MJO events do not lead to wintertime flooding over California, it is of interest to understand what if anything was unique about this event. We believe the answer to that question has less to do with any unique properties of this particular MJO and more to do with the underlying causes of PNA-like disturbances. PNA-like disturbances develop regardless of any MJO impacts as a result of the barotropic instability of the North Pacific jet (Simmons et al. 1988), and this appears to be enhanced during La Nina events which tend to produce more stunted jets (Schubert et al. 2001). The impact of that is best illustrated by Fig. 3 which shows a large intra-ensemble scatter in the flood region precipitation for our tropical replay runs with values ranging between about -2 and 10 mm/day. It is important to remember that each of those RPL_TR realizations (the red dots in Fig. 3) represents an equally likely outcome for simulations in which the tropics (including the MJO) is essentially perfectly known. To highlight this, Figure S6 compares the RPL_TR precipitation and circulation anomalies for the 5 ensemble members with the most and least precipitation in the flood region, showing the importance of the extension of the jet onto the coast in the flooding cases. Comparing the RPL_TR results with the NORPL results (the black dots in Fig. 3), we see that the impact of the tropics/MJO is to both shift the ensemble mean toward wetter (though likely not flooding) conditions, and increase the ensemble spread, which together increases the probability of the flooding event. It is nevertheless still an unlikely (extreme) outcome.

We can also point to the underlying sensitivity of PNA-like disturbances to the location of the vorticity forcing along the southern flank of the North Pacific jet exit region (Fig. 9c). It is

Accepted for publication in *Journal of Climate.* DOI 10.1175/JCLI-D-23-0696.1.

sobering to note that a relatively small shift of the positive vorticity forcing to the east of where it actually occurred, would presumably have led to a response of opposite sign (a negative PNA-like pattern).

Finally, while we cannot rule out the possibility that there was something especially unique about the MJO event itself (especially given the La Nina environment), it is worth noting that both the anomalous precipitation couplet straddling the equator in the eastern Indian Ocean and the development of a positive RWS (associated with the stretching term) in the jet entrance region that appears to have initiated this event (Fig. S2), are not inconsistent with the canonical characteristics of a phase 3 MJO as described in Wang et al. (2020). Furthermore, while the MJO was not particularly strong in mid-December of 2022, it persisted in the eastern Indian Ocean sector for quite some time[9], shifting between phases 3 and 4 - phases that tend to produce some of the most robust positive PNA-like responses (Wang et al. 2020).

With the above in mind, understanding the predictability of the flooding appears to be fundamentally tied to understanding the predictability of two key events. The first is the mid-December forcing of the ISW by the MJO and the second is the late December forcing of the positive PNA by the mature ISW. This suggests, first of all, that forecasts initialized well before mid-December will have no skill simply due to the limited predictability of the MJO (current skill is limited to one month or so, e.g., Vitart 2017). Forecasts with our coupled model (see also Deflorio et al. 2023) are not inconsistent with the above findings, showing little skill for forecasts initialized prior to about Dec 17. Most surprising is the greater skill for our forecasts initialized on December 22 compared with those initialized on December 27. While reasons for that are not well understood, it is noteworthy that the December 22 forecasts were initialized at the time the ISW reached its mature phase, while the December 27 forecasts were initialized at a time the positive PNA was just developing. Improving our understanding of such sensitivity to the initial conditions illustrates both the challenge and promise of predicting forecasts of opportunity (Mariotti et al. 2020).

Finally, we note that heavy rains continued to impact various locations along the west coast of North America during February and March, though these events do not appear to reflect a

Accepted for publication in *Journal of Climate.* DOI 10.1175/JCLI-D-23-0696.1.

continuation of the pronounced positive PNA-like circulation anomaly studied here, and so are presumably distinct and worthy of separate study.

Accepted for publication in *Journal of Climate.* DOI 10.1175/JCLI-D-23-0696.1.

Appendix: Derivation of the forcing sensitivity maps

Here we describe our approach to summarizing the large collection of SWM responses to idealized forcing imposed at regular locations (introduced in section 2.b). The responses to forcing at a given location are considered only over a target region of interest (e.g., the North Pacific and North America), defined by a set of m=1, M grid points. The individual forcing locations that correspond to each SWM simulation are defined by another set of n =1, N grid points. The ultimate goal is to identify those forcing locations (among the total N) that produce SWM responses most strongly resembling the observed anomaly in the target region (e.g., the PNA). We shall refer to those identified forcing locations and their relative degree of importance as a "forcing sensitivity map". To do this we first perform an empirical orthogonal function (EOF) analysis on the collection of SWM responses (we do this separately for the heating and vorticity forcing experiments). The corresponding MxM covariance matrix *G* is defined as the following:

$$G = F^T F, \tag{A1}$$

where F is an NxM matrix in which the nth row represents the SWM response map (i.e., the stream function response at each of the M locations of the target region) to forcing at point (n). Then, a standard eigenvector-eigenvalue problem is applied to the matrix *G* to obtain the EOFs:

$$GE = G\Gamma, \tag{A2}$$

where *E* is the MxM matrix of eigenvectors (i.e., the EOFs) and Γ is a diagonal matrix of the (m=1, M) eigenvalues (γ_m). The principal components (PCs, or *P*) are given by

$$P = FE. \tag{A3}$$

In the above, the leading EOFs (those with the largest eigenvalues or variances) represent the key modes of variability (across the SWM simulations) of the SWM responses over the target region, and the PCs are the projections of each SWM response onto the EOFs. As such, the PCs represent the agreement between the SWM responses (again, each corresponding to imposed idealized forcing at a given location) and the EOFs and form the basis for our forcing sensitivity maps.

Now all that remains is to determine the extent to which the EOFs resemble the observed target anomaly ($\vec{o}$). This agreement is defined, for the jth EOF ($\vec{e_j}$), as the spatial inner product

Accepted for publication in *Journal of Climate.* DOI 10.1175/JCLI-D-23-0696.1.

$$c_j = \vec{e}_j^{\,T}\vec{o}, \tag{A4}$$

where the arrows denote column vectors of length M, and the superscript T a transpose. The sensitivity maps, which are computed here using the leading four EOFs (typically explaining about 90% of the variance of the responses in the target region), are then defined as

$$\vec{s} = \frac{1}{a}\sum_{j=1}^{4}\frac{c_j\vec{P}_j}{\sqrt{\gamma_j}}, \tag{A5}$$

where $\vec{s}$ is a vector of length N representing the forcing sensitivities at each of N idealized forcing locations, $\vec{P}_j$ is the PC vector of length N for the jth EOF, and γ_j is the eigenvalue for the jth EOF. The above final result has a normalizing factor a, which represents the largest magnitude value of the quantity $\sum_{j=1}^{4}\frac{c_j\vec{P}_j}{\sqrt{\gamma_j}}$ over the N forcing locations. Also, the PCs are normalized by $\sqrt{\gamma_j}$ to place less emphasis on the variance explained by the EOF modes and more emphasis on the agreement of the EOF patterns with observations (c_j). In essence, the values in $\vec{s}$ are determined by 1) the degree of agreement between each SWM response and EOF (i.e., the normalized PCs) and 2) the degree to which each EOF resembles the observed target anomaly pattern, thus representing the extent to which each SWM response (to forcing at location n) resembles the observed pattern. The final vector $\vec{s}$ can be represented with a map, as each element corresponds to a different location (lon, lat) at which idealized forcing was applied.

Acknowledgments

This work was supported by the NASA MAP (NNG17HP01C and 80NSSC21K1729) program and the National Climate Assessment Enabling Tools project at NASA's Global Modeling and Assimilation Office (GMAO). MERRA-2 data were developed by the NASA GMAO at the Goddard Space Flight Center (GSFC) under funding by the NASA MAP program. The file specifications for the MERRA-2 output are documented in Bosilovich (2016). The various MERRA-2 fields used for this study (GMAO 2015a; 2015b; 2015c; 2015d) include precipitation that is corrected with gauge and satellite observations (Reichle et al. 2017). Computational resources supporting this work were provided by the NASA High-End Computing (HEC) Program through the NASA Center for Climate Simulation (NCCS) at GSFC.

Accepted for publication in *Journal of Climate.* DOI 10.1175/JCLI-D-23-0696.1.

Data availability statement

MERRA-2 data are available from the Goddard Earth Science Data and Information Services Center (GES DISC) at https://disc.gsfc.nasa.gov. Output from the AGCM simulations can be made available upon request.

Accepted for publication in *Journal of Climate.* DOI 10.1175/JCLI-D-23-0696.1.

References

Bosilovich, M. G., R. Lucchesi, and M. Suarez, 2016: MERRA-2: File Specification. GMAO Office Note No. 9 (Version 1.1), 73 pp, available from http://gmao.gsfc.nasa.gov/pubs/office_notes/

Chang, Y., S. D. Schubert, R. D. Koster, A. M. Molod, and H. Wang, 2019: Tendency Bias Correction in Coupled and Uncoupled Global Climate Models with a Focus on Impacts over North America. J. Climate, 32, 639–661, https://doi.org/10.1175/JCLI-D-18-0598.1

Chen, J., Li, R., Xie, S., Wei, J. and Shi, J., 2023: Characteristics and mechanisms of long-lasting 2021–2022 summer Northeast Pacific warm blobs. Frontiers in Marine Science, 10, https://doi.org/10.3389/fmars.2023.1158932.

Collow, A. B. M., H. Mersiovsky, and M. G. Bosilovich, 2020: Large-Scale Influences on Atmospheric River–Induced Extreme Precipitation Events along the Coast of Washington State. J. Hydrometeor., 21, 2139–2156, https://doi.org/10.1175/JHM-D-19-0272.1.

DeAngelis, A. M., S. D. Schubert, Y. Chang, Y. Lim, R. D. Koster, H. Wang, and A. B. Marquardt Collow, 2023: Dynamical drivers of the exceptional warmth over Siberia during the spring of 2020. J. Climate, https://doi.org/10.1175/JCLI-D-22-0387.1, in press.

DeFlorio, M. J., and Coauthors, 2023: From California's extreme drought to major flooding: Evaluating and synthesizing experimental seasonal and subseasonal forecasts of landfalling atmospheric rivers and extreme precipitation during Winter 2022 - 2023. Bull. Amer. Meteor. Soc., https://doi.org/10.1175/BAMS-D-22-0208.1, in press.

Fish, M. A., J. M. Done, D. L. Swain, A. M. Wilson, A. C. Michaelis, P. B. Gibson, and F. M. Ralph, 2022: Large-Scale Environments of Successive Atmospheric River Events Leading to Compound Precipitation Extremes in California. J. Climate, 35, 1515–1536, https://doi.org/10.1175/JCLI-D-21-0168.1

Gelaro, R., and Coauthors, 2017: The Modern-Era Retrospective Analysis for Research and Applications, Version 2 (MERRA-2). J. Climate, 30, 5419–5454, https://doi.org/10.1175/JCLI-D-16-0758.1.

GMAO, 2015a: tavg1_2d_slv_Nx: 2d, 1-hourly, time-averaged, single-level, assimilation, single-level diagnostics, V5.12.4. Goddard Space Flight Center Distributed Active Archive Center (GSFC DAAC), accessed 1 February 2023, https://doi.org/10.5067/VJAFPLI1CSIV.

GMAO, 2015b: tavg1_2d_flx_Nx: 2d, 1-hourly, time-averaged, single-level, assimilation, surface flux diagnostics, V5.12.4. Goddard Space Flight Center Distributed Active Archive Center (GSFC DAAC), accessed 1 February 2023, https://doi.org/10.5067/7MCPBJ41Y0K6.

Accepted for publication in *Journal of Climate.* DOI 10.1175/JCLI-D-23-0696.1.

GMAO, 2015c: inst3_3d_asm_Np: 3d, 3-hourly, instantaneous, pressure-level, assimilation, assimilated meteorological fields, V5.12.4. Goddard Space Flight Center Distributed Active Archive Center (GSFC DAAC), accessed 1 February 2023, https://doi.org/10.5067/QBZ6MG944HW0.

GMAO, 2015d: tavg3_3d_tdt_Np: 3d, 3-hourly, time-averaged, pressure-level, assimilation, temperature tendencies, V5.12.4. Goddard Space Flight Center Distributed Active Archive Center (GSFC DAAC), accessed 1 February 2023, https://doi.org/10.5067/9NCR9DDDOPFI.

Gimeno L, Nieto R, Vázquez M and Lavers DA (2014) Atmospheric rivers: a mini-review. Front. Earth Sci. 2:2. doi: 10.3389/feart.2014.00002

Goss, M., S. Lee, S. B. Feldstein, and N. S. Diffenbaugh, 2018: Can ENSO-Like Convection Force an ENSO-Like Extratropical Response on Subseasonal Time Scales? J. Climate, 31, 8339–8349, https://doi.org/10.1175/JCLI-D-17-0771.1.

Griffies, S. (2012). Elements of the Modular Ocean Model (MOM). http://mdl-mom5.herokuapp.com/web/docs/project/MOM5_elements. Pdf.

Griffies, S., Gnanadesikan, A., Dixon, K. W., Dunne, J. P., Gerdes, R., Harrison, M. J., et al. (2005). Formulation of an ocean model for global climate simulations. Ocean Science, 1, 1025–1035.

Guirguis, K., Gershunov, A., Shulgina, T. et al. Atmospheric rivers impacting Northern California and their modulation by a variable climate. Clim Dyn 52, 6569–6583 (2019). https://doi.org/10.1007/s00382-018-4532-5

Jong, B.-T., M. Ting and R. Seager, 2016: El Niño's impact on California precipitation: seasonality, regionality, and El Niño intensity. Environ. Res. Lett. 11 054021. DOI : https://doi.org/10.1088/1748-9326/11/5/054021

Koster, R. D., Suarez, M. J., Ducharne, A., Stieglitz, M., & Kumar, P. (2000). A catchment-based approach to modeling land surface processes in a GCM, Part 1, Model structure. Journal of Geophysical Research, 105, 24,809–24,822. https://doi.org/10.1029/2000JD900327.

Liu, A. Z., M. Ting, and H. Wang, 1998: Maintenance of circulation anomalies during the 1988 drought and 1993 floods over the United States. *J. Atmos. Sci.*, **55**, 2810–2832.

Mariotti, A., C. Baggett, E.A. Barnes, E. Becker, A. Butler, D.C. Collins, P.A. Dirmeyer, L. Ferranti, N.C. Johnson, J. Jones, B.P. Kirtman, A.L. Lang, A. Molod, M. Newman, A.W. Robertson, S. Schubert, D.E. Waliser, and J. Albers, 2020: Windows of Opportunity for Skillful Forecasts Subseasonal to Seasonal and Beyond. *Bull. Amer. Meteor. Soc.*, **101**, E608–E625, https://doi.org/10.1175/BAMS-D-18-0326.1

Accepted for publication in *Journal of Climate.* DOI 10.1175/JCLI-D-23-0696.1.

Molod, A. M., L. Takacs, M. Suarez, and J. Bacmeister, 2015: Development of the GEOS-5 atmospheric general circulation model: evolution from MERRA to MERRA2. Geosci. Model Dev., 8, 1339-1356, doi:10.5194/gmd-8-1339-2015.

Molod, A., E. Hackert, Y. Vikhliaev, B. Zhao, D. Barahona, G. Vernieres, A. Borovikov, R. M. Kovach, J. Marshak, S. Schubert, Z. Li, Y.-K. Lim, L. C. Andrews, R. Cullather, R. Koster, D. Achuthavarier, J. Carton, L. Coy, J. L. M. Freire, K. M. Longo, K. Nakada, and S. Pawson, 2020. GEOS-S2S Version 2: The GMAO High Resolution Coupled Model and Assimilation System for Seasonal Prediction. J. Geophy. Res. - Atmos., 125, e2019JD031767. doi: 10.1029/2019JD031767

Pegion, K., Kirtman, B., Becker, E., Collins, D., LaJoie, E., Burgman, R., et al. (2019). The Subseasonal Experiment (SubX): A multi-model subseasonal prediction experiment. Bulletin of the American Meteorological Society, 100, 2043–2060. https://doi.org/10. 1175/BAMS-D-18-0270.1

Reichle, R. H., Q. Liu, R. D. Koster, C. S. Draper, S. P. P. Mahanama, and G. S. Partyka, 2017: Land Surface Precipitation in MERRA-2. J. Climate, 30, 1643–1664, https://doi.org/10.1175/JCLI-D-16-0570.1.

Rienecker, M. M., Rienecker, M. M., Todling, R., Bacmeister, J., Takacs, L., Liu, H. C., et al. (2008). The GEOS-5 data assimilation system: Documentation of versions 5.0.1 and 5.1.0, and 5.2.0 (NASA Tech. Rep.): Series on Global Modeling and Data Assimilation NASA/TM-2008-104606.

Sardeshmukh, P. D., and B. J. Hoskins, 1988: The Generation of Global Rotational Flow by Steady Idealized Tropical Divergence. J. Atmos. Sci., 45, 1228 -1251, https://doi.org/10.1175/1520-0469(1988)045<1228:TGOGRF>2.0.CO;2. .

Schubert, S. D., M. J. Suarez, Y. Chang, and G. Branstator, 2001: The Impact of ENSO on Extratropical Low-Frequency Noise in Seasonal Forecasts. J. Climate, 14, 2351–2365, https://doi.org/10.1175/1520-0442(2001)014<2351:TIOEOE>2.0.CO;2.

Schubert, S., H. Wang, and M. Suarez, 2011: Warm Season Subseasonal Variability and Climate Extremes in the Northern Hemisphere: The Role of Stationary Rossby Waves. J. Climate, 24, 4773–4792, https://doi.org/10.1175/JCLI-D-10-05035.1.

Schubert, S., A. Borovikov, Y-K. Lim, and A. Molod, 2019a: Ensemble Generation Strategies Employed in the GMAO GEOS-S2S Forecast System. Technical Report Series on Global Modeling and Data Assimilation, Randal D. Koster, editor. NASA/TM-2019-104606, Vol. 53, 65 pp.

Schubert, S. D., Y. Chang, H. Wang, R. D. Koster, and A. M. Molod, 2019b: A Systematic Approach to Assessing the Sources and Global Impacts of Errors in Climate Models. J. Climate, 32, 8301–8321, https://doi.org/10.1175/JCLI-D-19-0189.1.

Accepted for publication in *Journal of Climate.* DOI 10.1175/JCLI-D-23-0696.1.

Schubert, S. D., Y. Chang, A. M. DeAngelis, H. Wang, and R. D. Koster, 2021: On the Development and Demise of the Fall 2019 Southeast U.S. Flash Drought: Links to an Extreme Positive IOD. J. Climate, 34, 1701–1723, https://doi.org/10.1175/JCLI-D-20-0428.1.

Schubert, S. D., Y. Chang, A. M. DeAngelis, R. D. Koster, Y. Lim, and H. Wang, 2022: Exceptional Warmth in the Northern Hemisphere during January–March of 2020: The Roles of Unforced and Forced Modes of Atmospheric Variability. J. Climate, 35, 2565–2584, https://doi.org/10.1175/JCLI-D-21-0291.1.

Simmons, A. J., J. M. Wallace, and G. W. Branstator, 1983: Barotropic Wave Propagation and Instability, and Atmospheric Teleconnection Patterns. J. Atmos. Sci., 40, 1363–1392, https://doi.org/10.1175/1520-0469(1983)040<1363:BWPAIA>2.0.CO;2.

Straus, D. M., and J. Shukla, 2002: Does ENSO Force the PNA?. J. Climate, 15, 2340–2358, https://doi.org/10.1175/1520-0442(2002)015<2340:DEFTP>2.0.CO;2.

Ting, M., and L. Yu, 1998: Steady Response to Tropical Heating in Wavy Linear and Nonlinear Baroclinic Models. J. Atmos. Sci., 55, 3565–3582, https://doi.org/10.1175/1520-0469(1998)055<3565:SRTTHI>2.0.CO;2.

Toride, K., and G. J. Hakim, 2022: What Distinguishes MJO Events Associated with Atmospheric Rivers?. J. Climate, 35, 6135–6149, https://doi.org/10.1175/JCLI-D-21-0493.1.

Uccellini, L. W., and D. R. Johnson, 1979: The Coupling of Upper and Lower Tropospheric Jet Streaks and Implications for the Development of Severe Convective Storms. Mon. Wea. Rev., 107, 682–703, https://doi.org/10.1175/1520-0493(1979)107<0682:TCOUAL>2.0.CO;2.

Vitart, F., 2017: Madden-Julian Oscillation prediction and teleconnections in the S2S database, Q. J. R. Meteorol. Soc., 143, 2210–2220.

Wallace, J. M., and D. S. Gutzler, 1981: Teleconnections in the Geopotential Height Field during the Northern Hemisphere Winter. Mon. Wea. Rev., 109, 784–812, https://doi.org/10.1175/1520-0493(1981)109<0784:TITGHF>2.0.CO;2.

Wang, B., Liu, F. & Chen, G. A trio-interaction theory for Madden–Julian oscillation. Geosci. Lett. 3, 34 (2016). https://doi.org/10.1186/s40562-016-0066-z

Wang, H., and M. Ting, 1999: Seasonal Cycle of the Climatological Stationary Waves in the NCEP–NCAR Reanalysis. J. Atmos. Sci., 56, 3892–3919, https://doi.org/10.1175/1520-0469(1999)056<3892:SCOTCS>2.0.CO;2.

Wang, J., H. Kim, D. Kim, S. A. Henderson, C. Stan, and E. D. Maloney, 2020: MJO Teleconnections over the PNA Region in Climate Models. Part I: Performance- and Process-Based Skill Metrics. J. Climate, 33, 1051–1067, https://doi.org/10.1175/JCLI-D-19-0253.1.

Accepted for publication in *Journal of Climate.* DOI 10.1175/JCLI-D-23-0696.1.

Zhou, Y., Kim, H., & Waliser, D. E. (2021). Atmospheric river lifecycle responses to the Madden-Julian Oscillation. Geophysical Research Letters, 48, e2020GL090983. https://doi.org/10.1029/2020GL090983.

Accepted for publication in *Journal of Climate.* DOI 10.1175/JCLI-D-23-0696.1.